OptoSkin: Novel LIDAR Touch Sensors for Detection of Touch and Pressure Within Wave Guides

Emmanuel Bacher, Sergio Cartiel, Jorge García-Pueyo, Julija Stopar, Aleš Zore, Roman Kamnik, *Member, IEEE*, Ilze Aulika, Andrejs Ogurcovs, Jurģis Grūbe, Arturs Bundulis, Jelena Butikova, Meldra Kemere, Adolfo Muñoz, and Martin Laurenzis

***Abstract*—Light detection and ranging (LIDAR) sensors, employing direct time-of-flight (dToF) measurements, are crucial for precise surface localization and are increasingly integrated into compact chip designs. These sensors have extensive use in proximity sensing in various applications. This article presents the innovative use of LIDAR sensors for ranging within waveguides to accurately detect touch and pressure. In our OptoSkin sensors, light propagates via total internal reflection (TIR) within the waveguide. Then, it is reflected back to the sensor as a result of waveguide deformation and/or scattering in the contact area, a phenomenon attributed to frustrated total internal reflection (FTIR). We have designed, simulated, and implemented different OptoSkin sensors using waveguides constructed from a flexible rod, rigid-curved 3-D-printed resin, and planar soft silicone rubber, respectively. Each configuration is equipped with multiple LIDAR sensors, demonstrating effective localization of touch points. In addition, pressure sensing was performed on the elastic wave guides. These novel touch sensors show great potential for applications such as robotic sensor skins, which enhance tactile responsiveness and interaction.**

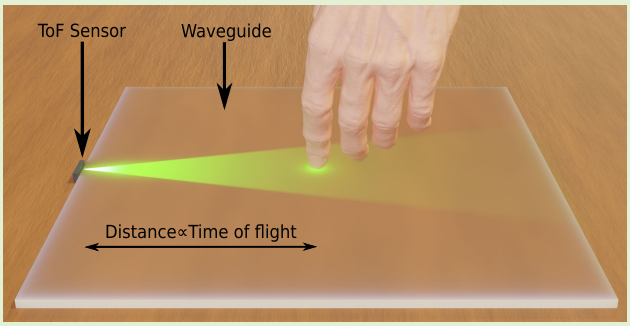

***Index Terms*— Frustrated total internal reflection (FTIR), light detection and ranging (LIDAR), light guide, optical sensing, proximity sensing, robotic sensor skin, tactile sensing, time-of-flight (ToF), touch detection, waveguide.**

I. Introduction

FRUSTRATED total internal reflection (FTIR) tactile sensors exploit light behavior to precisely detect touch and pressure. These sensors operate on the principle of light being totally reflected within a transparent medium until an object interferes, facilitating the measurement of touch location, force, and shape. All touch sensors based on FTIR described in the literature exhibit two primary configurations: first, the light detector directly observes the contact point [1], [2], [3], [4], [5], [6], [7], and second, the light detector laterally observes the contact point [7], [8], [9], [10], [11] within a defined sensing area. The spatial resolution of these sensors varies from approximately 0.1 to 5 mm, while the sensing area ranges from about 20 × 20 to 300 × 300 mm, respectively.

These FTIR touch sensor solutions typically require multiple light emitters and receivers to cover relatively large areas. Additionally, some designs necessitate complex material shapes, such as custom-built wedge-shaped optically transparent acrylic prisms to function as optical wave guides [9]. Furthermore, in the case of time-of-flight (ToF) fiber touch sensors, a complex waveguide configuration is suggested, where one end of the fiber is connected to the ToF light source for input, and the other end serves as output for the ToF detector [11].

Nevertheless, FTIR sensors are highly sensitive and capable of simultaneously detecting multiple touch points and object

Manuscript received 24 June 2024; revised 30 July 2024; accepted 1 August 2024. Date of publication 20 August 2024; date of current version 16 October 2024. This work was supported in part by the European Commission's Horizon Europe Research and Innovation Actions under Grant 101070310; and in part by the Institute of Solid State Physics, University of Latvia, through the Horizon 2020 Teaming Phase 2 Project Beneficiary, Centre of Excellence in Advanced Material Research and Technology (CAMART2), funded by the European Union, under Grant 739508. The associate editor coordinating the review of this article and approving it for publication was Dr. Qiang Wu. *(All authors contributed equally to this work.) (Corresponding author: Martin Laurenzis.)*

Emmanuel Bacher and Martin Laurenzis are with the French-German Research Institute of Saint-Louis, 68301 Saint-Louis, France (e-mail: martin.laurenzis@isl.eu).

Sergio Cartiel, Jorge García-Pueyo, and Adolfo Muñoz are with the Department of Computer Science and Systems Engineering, University of Zaragoza, 50019 Zaragoza, Spain (e-mail: adolfo@unizar.es).

Julija Stopar, Aleš Zore, and Roman Kamnik are with the Faculty of Electrical Engineering, University of Ljubljana, 1000 Ljubljana, Slovenia (e-mail: roman.kamnik@fe.uni-lj.si).

Ilze Aulika, Andrejs Ogurcovs, Jurģis Grūbe, Arturs Bundulis, Jelena Butikova, and Meldra Kemere are with the Institute of Solid State Physics, University of Latvia, 1063 Riga, Latvia (e-mail: aulika@cfi.lu.lv).

Digital Object Identifier 10.1109/JSEN.2024.3443615

shapes, making them ideal for applications in robotics for grippers, which require sensor equipment in compact spaces. However, they are sensitive to external light conditions and require controlled environments to avoid calibration issues. The materials used can also limit their effectiveness, and their complex data processing needs can be computationally intensive.

In this article, we present the OptoSkin sensor, a novel system that merges multiple light detection and ranging (LIDAR) sensors with a quasi-2-D optical waveguide. Light propagation within this waveguide is based on total internal reflection (TIR). Our method entails conducting range measurements within the waveguide to accurately detect both the position and pressure exerted during tactile interactions, resulting in scattering phenomena via FTIR. Additionally, the direct time-of-flight (dToF) range measuring through time-correlated single-photon counting exhibits minimal sensitivity to ambient light, facilitating the simultaneous operation of numerous sensors at the same laser wavelength [12] without significant interference.

In contrast to electrical sensing methods (such as capacitive or resistive sensing), our sensor surface does not require the integration of electrodes or dielectric multilayers. Additionally, there is no necessity for an extensive sensor matrix to monitor a large area. Similar to other optical tactile sensor technologies, our sensing method can detect multitouch and pressure. Our approach employs ToF sensing within a waveguide and computational reconstruction of the contact area. This technique enables us to adapt our sensing method to various applications. We can alter the surface of our OptoSkin sensor to many shapes and do not depend on special or multilayer designs. Our focus is on developing large-area sensor skins to cover various mechanical structures such as robot arms.

II. Sensing Principle

We propose an original solution by integrating ToF sensors with wave-guiding material to enhance the performance of FTIR touch sensors. This integration aims to create the OptoSkin touch sensor platform, offering simplicity, durability, reliability, and immunity to external light conditions. This fresh approach aims to address traditional FTIR sensor limitations, particularly in achieving precise touch detection across large surfaces while maintaining speed and efficiency. This advancement holds promise in improving the versatility and practicality of touch-interface technologies. Sections II-A–II-E, we elaborate on the underlying processes.

A. ToF Sensors

ToF sensors measure the distance between the sensor and an object by measuring the travel time of an emitted signal. Optical ToF sensors are composed of a light-emitting component, such as a vertical cavity surface-emitting laser (VCSEL), and a photo-sensor component, such as a single-photon-counting avalanche diode (SPAD). Depending on the underlying technology, ToF sensors can be divided into dToF sensors that directly measure the travel time of the pulsed light and indirect time-of-flight (iToF) that emit light in a modulated pattern and calculate the shift in the measurement, computing the distance as a postprocessing step (see the work of Piron et al. [13] for a more in-depth review about ToF sensors).

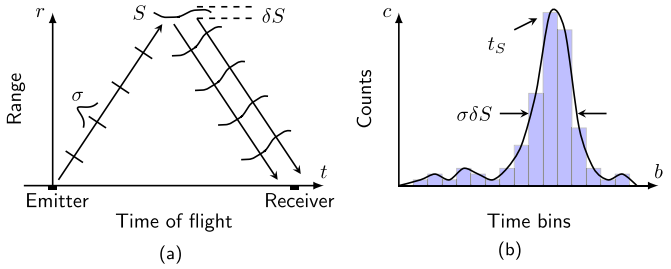

Fig. 1. (a) Time–range diagram illustrates the ToF measurement process. The scene S is illuminated by a light pulse σ, the returning light is recorded, and the round-trip time t_S is measured. Using single-photon-counting devices, (b) transient signal is formed as a histogram of many single measurements. The signal has a width that is determined by the width of the instrument response (dominated by the light pulse σ and the sensor resolution) and the geometry of the observed scene δS.

We are interested in dToF sensors that emit a short pulse of light with a width of σ toward the objects in the scene S, scatters back, and arrives to the sensor. In these devices, emitter and sensor are co-located on the same chip. Fig. 1(a) illustrates this time of flight of a light pulse in a time–range diagram. As the SPAD sensor can measure the time of a single event, the measurement must be repeated to be statistically reliable. Thus, the dToF sensor outputs histograms of counted events along time [see Fig. 1(b)]. These statistical measurements are processed to choose the time bin that corresponds to the measured object.

From the histogram, the ToF algorithms choose the time t_{ToF} associated with the round-trip time of the light from the sensor to the object (e.g., the time associated with the maximum value of the histogram). The distance d between the sensor and the object is proportional to t_{ToF} measured by the ToF sensor and is computed as

$$d = \frac{t_{\mathrm{ToF}}}{2} c \tag{1}$$

where c is the speed of light.

The distance measurement resolution Δd that we can obtain depends on the time resolution Δt_{ToF} of the ToF sensor and can be computed by applying Δt_{ToF} and Δd to (1). This means that for a centimeter resolution in the measured distance, the ToF sensor must have picosecond time resolution. In addition, ToF sensors also have an angular range and resolution that depends on the field-of-illumination (FoI) of the emitting component, and on the field-of-view (FoV) and pixel resolution of the photo-sensor component.

B. Optical Waveguide

In a vacuum, the speed of light is a general constant, $c_0 \approx 3 * 10^8$ (m/s). However, in a medium light, propagation depends on the optical density of the carrier medium. For instance, light travels slower in denser mediums like glass or water than in air. The index of refraction n_i of a medium

i is the ratio of the speed of light in vacuum c_0 compared to the speed of light in the medium c_i ($n_i = c_0/c_i$), so a medium with a higher index of refraction indicates slower light propagation.

When the light propagation path intersects with a different medium, part of the light is reflected and part of the light is transmitted to the new medium. This new medium has a different index of refraction, and the speed of light changes according to

$$c_2 = \frac{n_1}{n_2} c_1 \tag{2}$$

where n_1 and n_2 are the indices of refraction, and c_1 and c_2 are the speeds of light in the origin (carrier) and new (recipient) mediums, respectively. The part of the light that enters the new medium is refracted relative to the surface orientation (normal vector), according to Snell's law

$$n_1 \sin\theta_1 = n_2 \sin\theta_2 \tag{3}$$

where θ_1 is the angle of incidence and θ_2 is the angle of refraction.

When light passes from a medium with a higher index of refraction to another one with a lower index of refraction, $n_1 > n_2$, then TIR might happen if the incidence angle θ_1 is greater or equal to a critical angle θ_c

$$\theta_1 \geq \theta_c = \arcsin \frac{n_2}{n_1}. \tag{4}$$

In that case, light is completely reflected back into the original medium, without refracting. At lower angles ($\theta_1 < \theta_c$), the light is subject to reflection and transmission, as mentioned above and described in the Fresnel formula [14].

TIR is the principle used by optical wave guides, such as optical fibers, for lossless or low-loss transmission of optical signals. Typically, an optical fiber is composed of a carrier material with a high index of refraction, called the core, surrounded by a low index of refraction material, called the cladding. Our waveguides will use only the carrier material with a higher index of refraction than the surrounding air.

C. ToF Sensors in an Optical Waveguide

The proposed touch sensing technology is made up of dToF sensors attached to optical wave-guiding materials. The light emitted by the dToF sensor enters the optical waveguide, is propagated inside by TIR, and reaches the end of the optical waveguide. Part of the light is refracted outside the waveguide material, and part is reflected back inside the material, to be propagated in the opposite direction in the optical waveguide until reaching the ToF sensor [Fig. 2(a)].

ToF sensor algorithms to compute object distance based on the captured histogram assume that light is propagated in an open space composed of air, but this assumption is no valid in our setup as light propagated through the waveguide medium. Further, light propagation changes direction when the light enters or exits the optical waveguide due to Snell's law [see (3)]. This effect impacts the FoI and FoV of the ToF sensor to the same extent. If we assume that the index of refraction of air $n_0 \approx 1$, the index of refraction of the

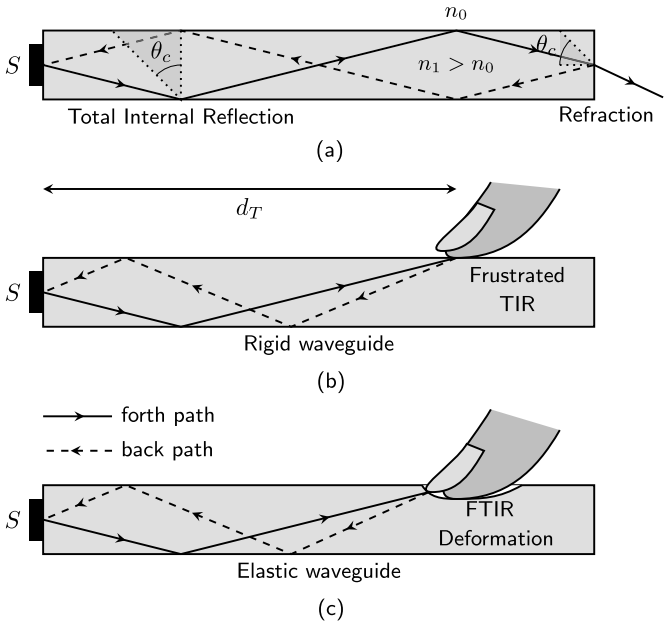

Fig. 2. Within the OptoSkin, light is propagating through the waveguide by (a) TIR ($n_0 < n_1$). In the touched area, light is reflected by (b) interaction of light with environment ($n_2 \neq n_0$) through frustrated total reflection conditions, e.g., scattering from skin ($n_2 \approx n_1$) and due to (c) deformation (elastic material) of the waveguide surface.

waveguide n_1, and the original FoI/FoV angle of the ToF sensor θ_0, the effective FoI/FoV angle inside the optical waveguide θ_1 is

$$\theta_1 = \arcsin\left(\frac{n_0}{n_1}\sin(\theta_0)\right). \tag{5}$$

Moreover, we have to modify the computed distance from the sensor to the object from the round-trip time [see (1)] as

$$d = \frac{t_{\text{ToF}}}{2} c_1 = \frac{t_{\text{ToF}}}{2} \frac{n_0}{n_1} c_0 \text{ with } n_1 > n_0 \tag{6}$$

taking into account the speed of light inside the optical waveguide c_1 according to (2). The higher index of refraction of the waveguide material ($n_1 > n_0$) provides an increased distance resolution Δd, maintaining the time resolution of the ToF sensor Δt_{ToF}, which can be computed applying Δd and Δt_{ToF} to (6).

On the other hand, the optical power P_R received by the sensor depends on the optical power emitted P_T and its propagation through the material. The optical power density is attenuated due to divergent illumination and reflection, scattering, and absorption. P_R can be calculated from the LIDAR equation, as found in many textbooks [15], [16]

$$P_R \propto \rho \frac{\eta_{\text{atm}}^2}{R^2} \tag{7}$$

with R the detection range and $\eta_{\text{atm}}^2 = e^{-2\mu R}$ describing the two-path attenuation process (illumination and reception paths) in the propagation medium, here, the atmosphere. Hence, $\mu = \mu_{\text{sc}} + \mu_{\text{abs}}$ is the atmospheric attenuation coefficient describing the absorption and scattering processes.

In the air [see Fig. 3(a)], the atmospheric attenuation coefficient μ is low to attain a visibility on the meter-to-kilometer

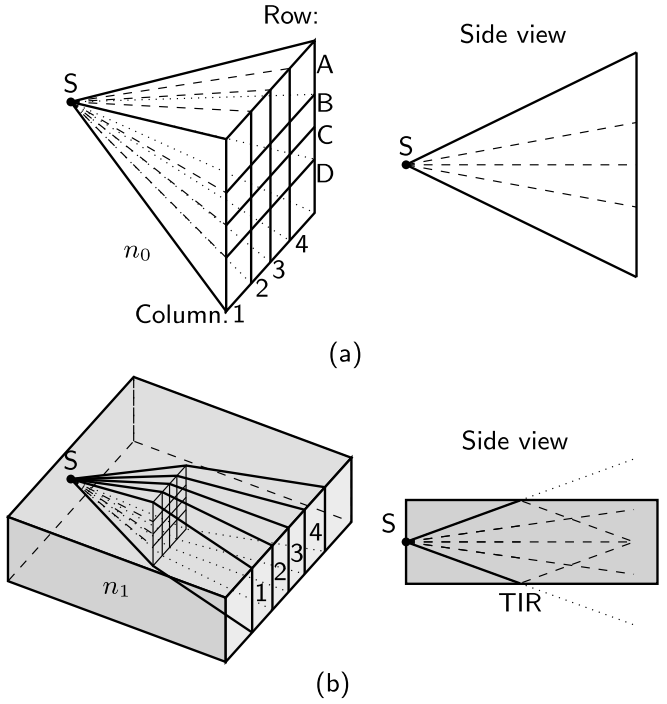

Fig. 3. Illustration of the sensor's FoV (a) in air and (b) in an optical waveguide. Due to TIR, in (b), the signals mix along the columns of the sensor array.

scale. Here, the dominant attenuation process that limits the maximum detection range is due to the divergence of the laser source ($1/R^2$) component.

Due to the TIR in our waveguide, the divergence of the light is limited in one direction [see Fig. 3(b)], so that the $1/R^2$ attenuation is not valid in our case. However, due to the strong scattering of light in the polymer material, its divergence can be neglected and the scattering described by η_{atm}^2 can be identified as the dominant process.

However, since the actual behavior of the signal strength as a function of distance is not known, we will later use reference measurements to normalize the measured signals and thus correct the dependence of the signal on the distance. In this way, we can also compensate for the material- and geometry-related inhomogeneities of the waveguide.

Additionally, as demonstrated in Fig. 3(b), it is unnecessary to employ the complete resolution of the sensor array because signal diffusion occurs along the columns due to TIR. Furthermore, we specify a sector for each column in the sensor array, as every column captures photons that return from a specific angle range denoted by $\theta_i \pm \delta\theta_i$. Here, θ_i represents the mean viewing angle of the ith sensor sector and $\delta\theta_i$ denotes the width of the reception area. Consequently, in later discussions of outcomes, we primarily consider the ToF sensor analogous to line sensors.

D. Touch Sensing

Two distinct mechanisms are utilized for touch sensing: one involves a waveguide constructed from a rigid material such as glass or resin, called the HardSkin sensor, and the other uses a waveguide made from an elastic material such as silicone rubber, referred to as the SoftSkin sensor. More information about these sensors can be found in Section IV. In both types of waveguides, TIR occurs when light meets an interface with a medium that has a lower refractive index (such as glass to air) and the incidence angle is larger than the critical angle.

In instances where another medium comes into contact with the waveguide interface, such as a human finger (considering that the refractive index of human skin is approximately equal to $n_{\text{human}} \approx 1.5$ [17], [18]), it can interfere with TIR and prompt light rays to refract and leave the waveguide. This phenomenon, known as FTIR, has found applications in multitouch screen sensing [3] and force sensors [19]. When the material-inducing FTIR (e.g., human skin) exhibits partial diffusion, it will scatter light in various directions, allowing some of the scattered light to reenter the waveguide and travel back toward the sensor, as illustrated in Fig. 2(b).

In this study, we harness FTIR for touch detection within the waveguide, as incoming light from the ToF sensor gets reflected back at the contact point, reaching the ToF sensor at t_{touch}. Consequently, the distance to the touch location, represented by d_{touch}, can be derived by utilizing (6).

In addition, if the material of the waveguide is elastic, it is deformed on contact, which changes its physical shape [see illustration in Fig. 2(c)]. In that case, the angle of incidence of the light, which previously created TIR, will be greater with respect to the normal at the locally modified surface and might cause light to refract outside the waveguide. Similar to before, if the material of the object causing the deformation is partly diffuse, it will scatter light in all directions and reflect back light to the ToF sensor. Note that while in the HardSkin approach, only the FTIR principle due to a change of interfaces is present, and in SoftSkin, both a change of interfaces and a change of the shape locally at the touch point are present.

E. Reconstruction of Touch Location

The touch location is reconstructed from the captured histogram, where touch is detected due to the reflected light that has arrived at the sensor from FTIR. We propose to create a sensor-centered likelihood heat map of touch by projecting the captured histogram on the surface of the planar waveguide, taking into account the angular coverage of the ToF sensor that depends on the FoV and FoI.

Assuming a very thin waveguide, we consider $z \approx 0$, so we can assume that the measured distance values (d) and the sensor sections (θ, the angle of reception) represent polar coordinates $\mathcal{P}_{d,\theta} = (d, \theta)$. These values can be transformed into Cartesian coordinates $\mathcal{C}_{x,y}$ by the transformation of the coordinate system

$$\mathcal{P}_{d,\theta} \rightarrow \mathcal{C}_{x,y} : x = d\cos(\theta) \qquad y = d\sin(\theta). \tag{8}$$

Let us further assume that we determine d and θ with a certain accuracy, which are denoted by the errors σ_d and σ_θ, respectively. Here, $\sigma_d \approx \Delta d$ is the range resolution of the sensor and $\sigma_\theta \approx \delta\theta$ is the angular width of the specific sensing section.

To transfer these errors to the Cartesian coordinates, we can use the following formulas:

$$\sigma_x = \sqrt{(\cos(\theta))^2\sigma_d^2 + (d\sin(\theta))^2\sigma_\theta^2} \tag{9}$$

$$\sigma_y = \sqrt{(\sin(\theta))^2\sigma_d^2 + (d\cos(\theta))^2\sigma_\theta^2}. \tag{10}$$

We can simplify (9) and (10) by using the small angle approximation ($\theta \to 0 : \cos(\theta) = 1, \sin(\theta) = 0$) to obtain the following expressions:

$$\sigma_x \approx \sigma_d \tag{11}$$

$$\sigma_y \approx d\sigma_\theta. \tag{12}$$

In setups using a single sensor, the precision in pinpointing the touch location along the x- and y-axes greatly depends on the ToF sensor's characteristics. The error in accuracy along the x-axis, denoted by σ_x, is primarily determined by the sensor's range resolution. In contrast, the accuracy error along the y-axis, denoted by σ_y, is related to the sensor FoV and increases proportionally with the measured distance, later expressed as a percentage of this distance.

In fact, there are discrepancies in the optical path lengths between multiple reflection paths and direct line-of-sight. Nevertheless, these disparities are too insignificant to be registered by our sensors. Moreover, we employ comparatively narrow waveguides, thereby eliminating the necessity to modify the propagation path for multiple reflection paths. Therefore, our reconstruction algorithm does not account for the curvature of the waveguide, regardless of whether it is curved or flat, and enables us to map the reconstructed data onto a 3-D model.

Thus, limiting the OptoSkin sensor size, the accuracy of our approach is sufficient for human–robot interaction (HRI) applications that require precise localization of touches, such as gesture recognition and robot manipulation. By investigating configurations that involve multiple ToF sensors, we expect to further refine the accuracy of touch localization.

III. Simulation

The sensing principle of OptoSkin, explained in the previous section, has initially been evaluated through physically-based simulation. This allows us to demonstrate the sensing principle under perfect and controllable conditions. Later, in Section IV, an experimental evaluation is performed.

The general simulation setup consists of an optical waveguide and one or multiple ToF sensors attached to it (Fig. 4). The waveguide materials of the simulation setup are transparent, without scattering or absorption, to test the sensing principle. We simulate the output histogram of the ToF sensor by using a modified version of the Mitsuba 3 rendering software [20] adapted for transient light transport [21], [22], being able to simulate the light's ToF. The transient data obtained from these simulations are similar to real sensor data and describe the returning signatures over time. Then, we apply the touch reconstruction algorithm described in Section II-E and obtain a likelihood heat map of touch [Fig. 5(a)].

Simulations facilitate the investigation of OptoSkin configurations under various conditions, such as changes in the ToF characteristics (time resolution, FoV, and FoI), arrangements of ToF sensors, waveguide geometries, and optical traits (for example, scattering and absorption). For example, in Fig. 5(b), two simultaneous touches are detected at different areas of the surface using an arrangement of six ToF sensors strategically placed [Fig. 4(b)]. Additionally, the simulation can include a waveguide made of an elastic material subjected to varying pressures, examining how changes in the waveguide's shape influence touch detection. Fig. 6 shows that the touch signal increases with greater deformation caused by increased pressure.

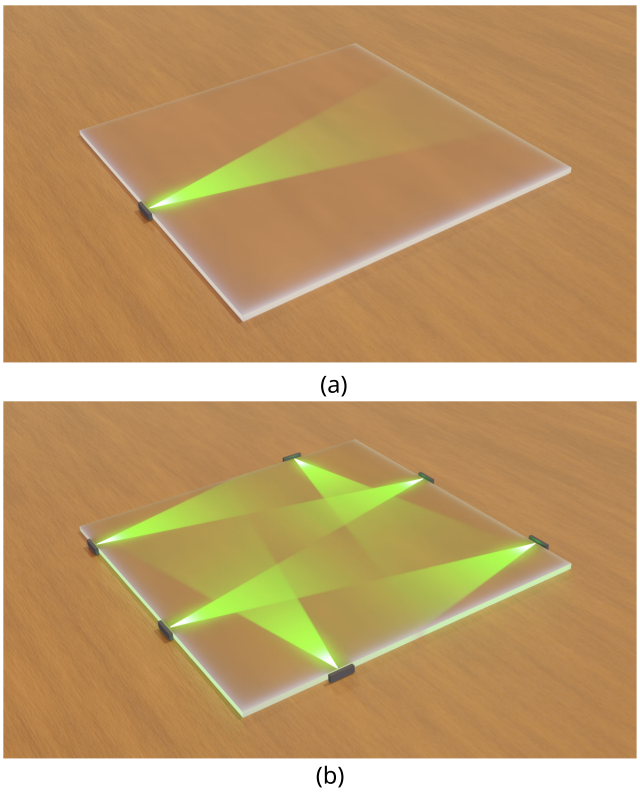

Fig. 4. Virtual representation of the setup used to simulate the OptoSkin sensing principle using different configurations of ToF sensors attached to the waveguide: (a) single sensor and (b) distribution of six sensors.

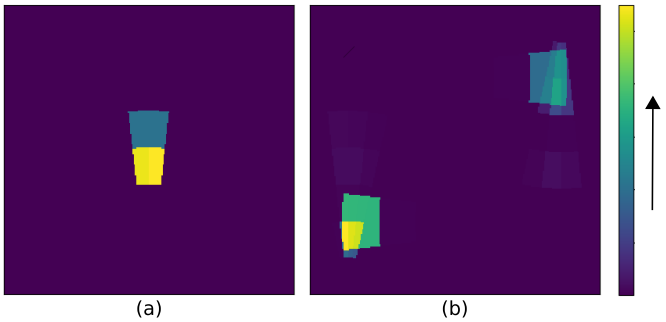

Fig. 5. Touch reconstruction on a HardSkin sensor: (a) one touch detected by a single ToF sensor and (b) dual touches detected using six ToF sensors.

IV. Experimental Investigation

A. Waveguide Material Selection

We investigated the optical and mechanical properties of different waveguide material candidates. All in all, we characterized a soft silicone rubber, 3-D-printed rigid

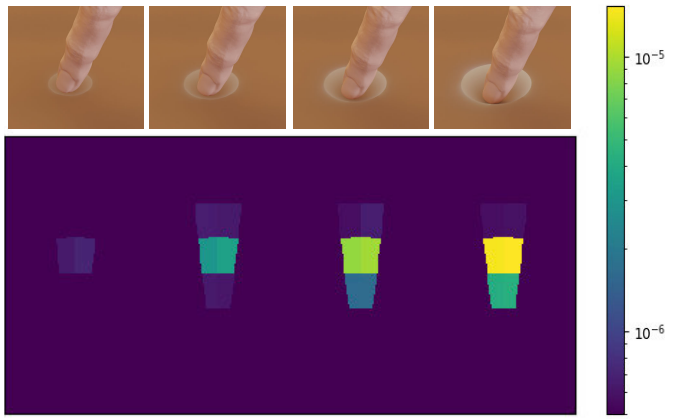

Fig. 6. Reconstruction of four touch events with increasing pressures in a SoftSkin waveguide.

photopolymer resins, and flexible poly-methyl-methacrylate (PMMA) fibers.

When light encounters inhomogeneities in the material, it can be scattered in various directions, leading to a reduction in the intensity of the transmitted light. Thus, the scattering coefficient μ_S is a measure of the scattering ability of inhomogeneities in the material, which scatteres optical power out of a light beam. In addition, the absorption coefficient μ_A quantifies the absorption of light by the medium itself. These coefficients are fundamental in fields such as optics, atmospheric science, and materials science, where understanding light interactions is essential for various applications.

We measured the transmittance T, reflectance R, and diffuse reflectance R_{dif} in a spectral range of 175–3300 nm using a universal measurement spectrometer (Cary 7000, Agilent, Santa Clara, CA, USA). The scattering coefficient μ_S was obtained according to guidelines of Foschum et al. [23] and Bergmann et al. [24].

Additionally, the Metricon Model 2010/M Prism Coupler [25] was utilized for atypical samples like 3-D-printed and flexible materials to determine the refractive index n at specific angles across three wavelengths (1064, 632.8, and 532 nm). In these instances, the refractive index at 940 nm was approximated by fitting the experimental data to Cauchy's equation $n = A + (B/\lambda^2) + (C/\lambda^4)$ [14], [26]. Additionally, the refractive index for silicone samples was measured using a spectral ellipsometer (RC2 – XI, J.A.Woollam, USA).

In Table I, the optical properties of selected waveguide materials are summarized. We present the measured refractive index n, the diffuse reflectance R_{dif}, the transmittance T, the absorption coefficient μ_A, and scattering coefficient μ_S are given at 940 nm. This wavelength corresponds to the typical emitter wavelength of ToF sensors. The 3-D-printed materials (rigid photopolymers) have a slightly higher refractive index n with respect to silicone rubber due to higher density. Further, the 3-D-printed materials have also larger diffuse reflectance R_{dif} due to higher surface roughness with respect to silicone rubber. All evaluated materials show similar transmittance T in the range from 82% to 88% due to low light scattering. The highest transmittance T and no light scattering were found for the PMMA flexible waveguide, providing ideal light guiding conditions.

TABLE I
EVALUATION OF SOME WAVEGUIDE MATERIAL CANDIDATES: PHOTOPOLYMERS FOR 3-D PRINTING, SILICONE RUBBER, AND PMMA

Name	n	R_{dif} [%]	T [%]	μ_A $[cm^{-1}]$	μ_S $[cm^{-1}]$	Comment
3D printed rigid photo-polymer resin						
Crystal Clear	1.483	6.6	88.6	0.1	0.2	transparent, clear
Tech Clear	1.537	7.4	82.1	0.14	0.8	transparent, blue
Clear Impact	1.523	7	82.5	0.15	1.1	transparent, yellow
Soft silicone rubber						
TFC4190-T19	1.400	4.9	84.4	0.14	0.6	transparent, clear
Crystalflex	1.398	1.9	88.2	0.06	0.1	transparent, clear
Flexible PMMA wave guide						
1216.1013	1.498	tbd	93.3	0	0	transparent, clear

TABLE II
EVALUATION OF SOME LOIC CHIPS WITH HISTOGRAMMING FUNCTION

Name	Sensor (Array)	Laser (λ)	FOV	Time bin width
AMS TMF8828	SPAD (8x8)	VCSEL (940nm)	$41\,^\circ \times 52\,^\circ$ $0.7\,\text{rad} \times 0.9\,\text{rad}$	100 ps/bin
STMicro. VL53L8	SPAD (8x8)	VCSEL (940nm)	$45\,^\circ \times 45\,^\circ$ $0.8\,\text{rad} \times 0.8\,\text{rad}$	250 ps/bin

Based on our examinations, we determined that using the PMMA Fiber (Mentor, Germany), the Tech Clear resin (Moiin, Germany) for 3-D printing and the silicone rubbers (TFC, Germany, and Samson Kamnik, Slovenia) for cast polymerization would be suitable for fabricating various OptoSkin sensors, namely, the SoftSkin and HardSkin prototypes.

B. Sensor Selection

At the time of this study, there were various commercially available integrated laser ranging sensors, known as LIDAR on integrated circuits (LoICs). A nonexhaustive list of these sensors can be found in Table II. These sensors are engineered to detect the proximity of surfaces by using a dToF laser ranging technique, as described in Section II-A. The sensors typically include a laser source for emitting light pulses and a highly sensitive detector to capture the returning echo. Generally, the sensor is built around a SPAD array, while the light source is a VCSEL, with both components integrated into a single silicon chip.

Generally, the laser emission is minimal, and the laser sources are classified as Laser Class 1 [27]. This ensures no damage to human eyes and eliminates the need for protective measures for the user (skin or eyes). Additionally, we did not detect any thermal effects from the waveguide's absorption of optical power.

Given that these sensors can detect individual photon events, they automatically execute thousands of separate measurements and provide the most likely range value. Moreover, certain models, such as the VL53L8 (STMicroelectronics, Switzerland) and TMF8828 (AMS-OSRAM, Austria), offer a histogram function that returns the signal's temporal profile. This feature is particularly beneficial when measuring in scattering environments, enabling users to apply custom advanced analysis algorithms. Both sensors possess sub-nanosecond time resolution; however, due to its high temporal resolution of 100 ps/bin, we opted to utilize the TMF8828 sensor for subsequent experimental investigations.

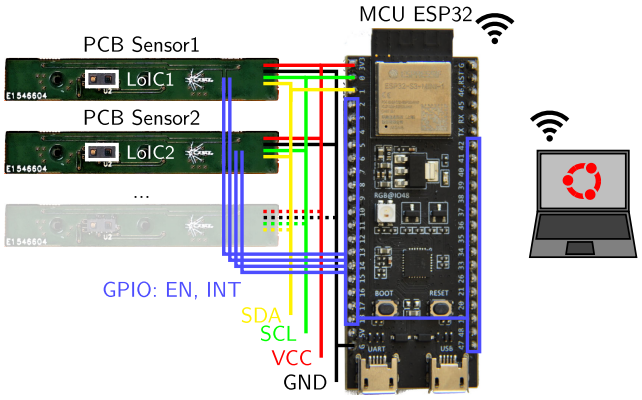

Fig. 7. Multiple laser ranging sensor modules (LoICs) can be controlled and read out by an MCU through separate I^{2}C communication lines.

TABLE III
REALIZED OPTOSKIN DEMONSTRATORS

Name	Material	Shape	Dimensions	σ_x	σ_y
Rod	PMMA	1D rod	l = 115 mm, d = 3 mm	1 cm	11.1 %
HardSkin	resin	2D curved	180 °, R = 60 mm, d = 5 mm	0.98 cm	10.8 %
SoftSkin 1	silicone	2D flat	30 cm × 30 cm, d = 5 mm	1.07 cm	11.9 %
SoftSkin 2	silicone	2D flat	30 cm × 30 cm, d = 10 mm	1.07 cm	11.9 %

C. Experimental Setups

Our setups consist of two main components, the electronics and the wave guides, and are described in detail in the following.

1) Electronic Boards: The electronic layout of our setups is sketched in Fig. 7. For each setup, we use a single microcontroller unit (MCU) (e.g., ESP32, Espressif Systems, and CN) to control and read out several sensors using the interintegrated circuit (I^{2}C) serial controller bus. The recorded data are processed in the MCU and transmitted to a main computer via a wireless network.

We realized small printed circuit boards (PCBs) equipped with a single sensor (LoIC) and driver electronics to install different sensors at the waveguides. In our setups, we use the TMF8828 proximity sensor, which is capable of returning by default histograms of the recorded signals. Each daughter board is connected to the MCU by joint power (VCC), ground (GND), I2C clock (SCL), and data (SDA) line. Further, each sensor has two individual connections: the enable bus (EN) is used to switch the individual sensors on and off, and the interrupt (INT) is used to receive messages from the sensor when new data are available.

2) Waveguides: We have realized four versions of the OptoSkin sensor, as depicted in Fig. 8, using different material (see Table I) and processing methods. The parameters of different setups are described in the following and are summarized in Table III. In the given configurations, we expect to localize the touch point within the sensor FoV with a precision of about $\sigma_x \approx (\Delta t_{\text{ToF}})/2(c/n_1) = 1$ cm and $\sigma_y \approx 0.1\ x$.

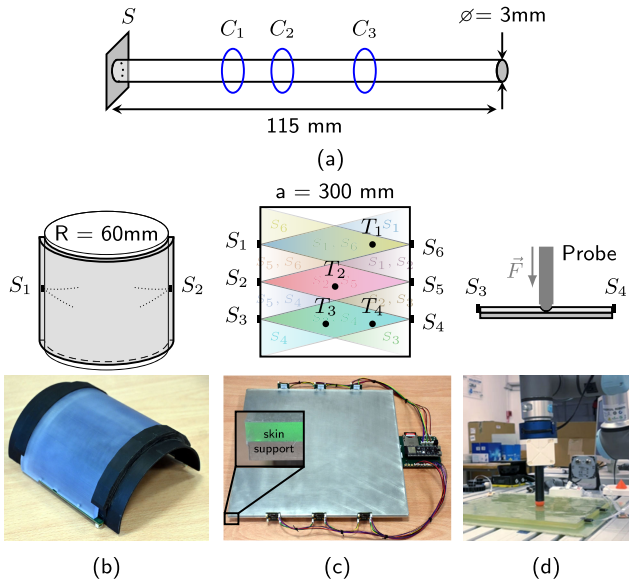

Fig. 8. Sketches and images of our technology demonstrators with (a) flexible PMMA rod, (b) 3-D-printed rigid optical waveguide (HardSkin), and (c) and (d) two SoftSkin models based on an elastic silicone rubber.

A first sensor, Fig. 8(a), consists of a 1-D rod made of flexible PMMA with a length of 115 mm and a diameter of 3 mm. This sensor can only sense the range of the touch and was used for the first investigation of touch sensing and to demonstrate the fundamental sensing principles.

A second sensor [Fig. 8(b)] has a rigid quasi-2-D waveguide made of hard resin (HardSkin). This waveguide was 3-D-printed in a photopolymerization process by layer-by-layer illumination with ultraviolet light (printer: Saturn 2, Elegoo, CN) using Tech Clear resin. We printed waveguides with various shapes and realized, among others, a curved waveguide with the shape of a semicylindrical hull with a radius of $R = 60$ mm and a curvature angle of 180°. The waveguide has a thickness of 5 mm, a height of 10 cm, and a curvature length of about 18.85 cm. We have mounted two sensors opposite each other, aligned tangentially to the curvature of the waveguide. In this configuration, the TIR bends the FoV along this curvature. The sensor was set up to cover a cylindrical support structure such as a robot arm (e.g., UR10).

In addition, we have set up two SoftSkin sensors consisting of waveguides made of elastic silicone rubber with the consistency of soft skin. The waveguides were created in a cast polymerization process by pouring the silicone onto a support structure (e.g., aluminum plate) during polymerization. The silicone waveguides had to dry (heal) for several hours before the sensors could be installed.

As shown in Fig. 8(c), the first SoftSkin sensor (SoftSkin 1) was made of TFC4190 silicon rubber with a stiffness of Shore 00-80 and has a dimension of 30 × 30 cm with a thickness of $d = 5$ mm. Six sensors have been installed, arranged in sets of three facing each other. In this configuration, the sensors' FoVs cover about 87.5% of the SoftSkin surface (25% covered by a single sensor and 62.5% covered with two sensors). We set up this sensor to demonstrate the application of multiple ToF sensors and to localize touch events.

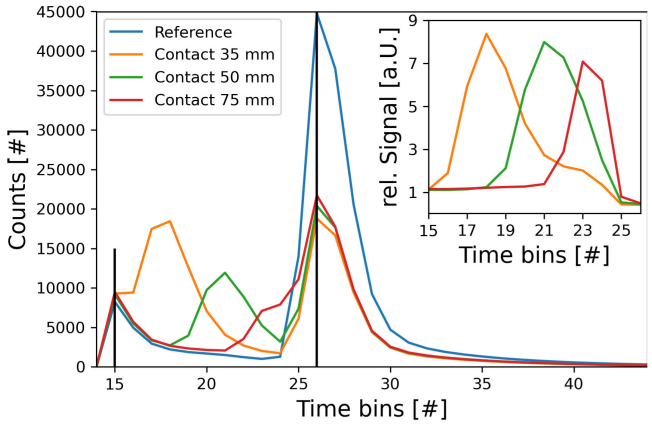

Fig. 9. Signatures of a finger touching the rod sensor at different contact points at distances C1 = 35 mm (orange), C2 = 50 mm (green), and C3 = 75 mm (red). The data are compared to the signature of the rod sensor without contact (blue). The inset shows the relative signal of the three touch events.

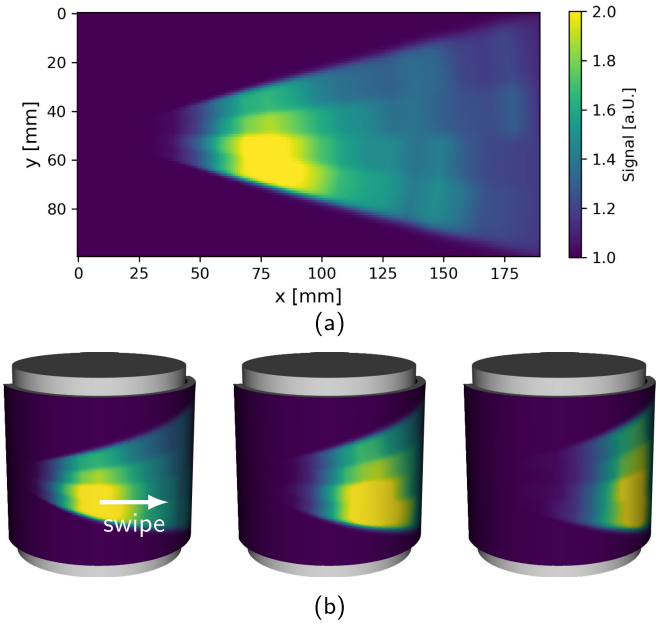

Fig. 10. Experimental results for the HardSkin demonstrator as (a) single 2-D color map showing a hand touching the sensor surface and (b) time series of color maps projected onto a 3-D model showing a swiping gesture.

The second SoftSkin sensor (SoftSkin 2), shown in Fig. 8(d), has the dimensions of 34 × 30 cm with a thickness of $d = 10$ mm. Along the two shorter sides, four ToF sensors are installed in a configuration that ensures maximal sensor FoV coverage and minimal overlap. Mechanical adapters, into which up to four removable ToF sensors may be inserted, are embedded into the silicone. Additionally, we detached the silicone rubber from the casting support structure, allowing the SoftSkin to be mounted on various supports and utilized in multiple configurations. This formulation allows the prototype to be deployed either in a flat configuration or wrapped around cylindrical objects, such as robot arm segments, while ensuring optimal contact between the ToF sensors and the silicone rubber.

D. Experimental Results

We used all four experimental setups to examine the ToF propagation in an optical waveguide with different focus depending on the specific sensor setup.

1) Rod Waveguide: The 1-D rod waveguide was used to investigate the underlying principle of detecting signatures from the interaction of the applied laser pulse with human tissue that are fingers touching or gripping the waveguide. The interaction process relies on FTIR that is light partly reflected within the waveguide and partly transmitted into the human tissue. Within the tissue, the light is diffused and scattered back into the waveguide. During this process, part of the laser light is scattered back toward the ToF sensor detecting the transient signal.

In Fig. 9, we show transient signals recorded without (blue) and with touching the rod waveguide at three different positions (orange, green, and red). In the reference signal (blue, without touch), we can observe peaks, at time bins of 15 and 26, which can be identified as reflections of the laser pulse at the waveguide's entrance and exit facets. These signatures are the background signals which specific to the applied waveguide and they are visible in all measurements.

Touching the waveguide gives additional responses mixing with the background signal. Clearly, the signal can be distinguished from reference for three different contact distances ($d \approx 35$, 50, and 75 mm). For better visibility, the relative signals are shown in the inset for time bins of interest ($b \in [15, 26]$). Further, in our investigations, we could show that this kind of touch sensing works with a bending curvature of the 1-D waveguide up to a diameter of 80 mm without affecting the signal and the contact point detection. This curvature is sufficient to cover mechanical structures such as robotic arms (e.g., UR10).

2) HardSkin: As mentioned above, the HardSkin sensor has a quasi-2-D waveguide with a semicylindrical curvature. Therefore, the recorded signatures can be displayed in a 2-D color map allowing us to localize the touch point on the skin surface. In the experiments, we used only one of the two mounted ToF sensors.

In Fig. 10(a), we show an exemplary result of a hand touching the HardSkin sensor. The 2-D heat map shows the relative location of the touch point as position along the surface range or tangential position (x) and the surface height (y). We can identify a single contact area at $x = 60$ mm and $y = 75$ mm.

In addition, the 2-D heat maps can be used to locate the touch point in 3-D space by the projection of maps onto a spatial model. In Fig. 10(b), we project heat maps onto a cylindrical surface model. Fig. 10(b) illustrates a time series of results showing the signature of a hand swiping over the sensor surface. Here, we can observe the movement of the contact point on the projection model and could analyze the gesture to control the robot. The 3-D model gives the exact position of the touch point in the robot model.

3) SoftSkin 1: The SoftSkin 1 sensor is a 2-D skin equipped with six ToF sensors. Each sensor was used to monitor a certain region of the sensor skin, and most of the sensor surface

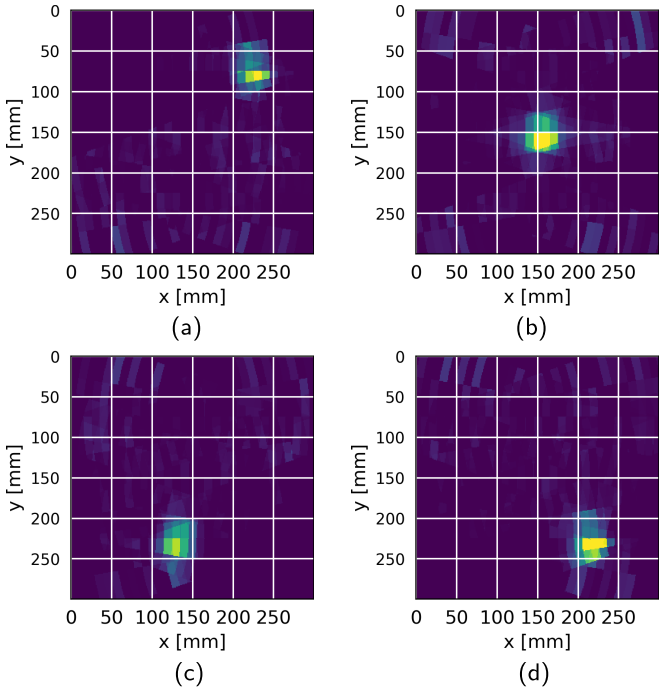

Fig. 11. Results for the SoftSkin 1 sensor to localize the touch point on the SkinSurface. We tested four different positions. (a) Upper right, (b) center, (c) lower center, and (d) lower right.

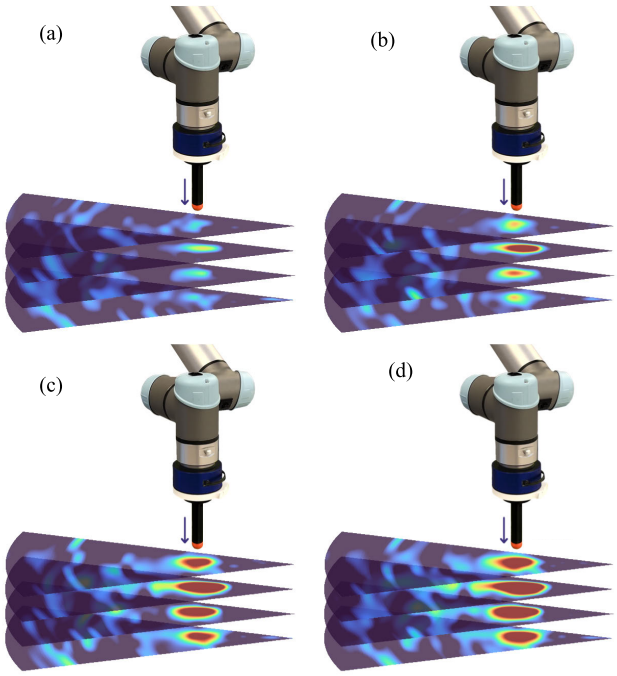

Fig. 12. Simultaneous localization and pressure sensing with the SoftSkin sensor. Diagrams show the sensor response as different contact force magnitudes: (a) 5 N; (b) 15 N; (c) 30 N; and (d) 45 N are being applied onto the skin with a probe.

was covered by at least one sensor. Therefore, the SoftSkin 1 sensor was set up to investigate the localization of touch points in a multisensor configuration.

In Fig. 11, we show a series of color maps showing the signature of a probe touching the sensor at different locations, T_1–T_4. In these cases [Fig. 11(a)–(d)], the touch event was detected only by the sensors dedicated for that specific skin surface region. The sensors did not return a signature if the touch event took place outside their FoV. Therefore, we could proof the reliability of the sensing process and the robustness against false detection events. Further, by combining touch sensing from different ToF sensors with different aspect angles, it is possible to enhance the precision of the localization to $\sigma_x < 1$ cm and $\sigma_y < 1.5$ cm.

4) SoftSkin 2: In addition to point-of-contact localization, we have investigated whether SoftSkin can be used to estimate the contact force applied to its surface. The underlying principle revolves around the use of FTIR to interpret sensor signals, which are influenced by both the contact surface area and the depth of surface deformation. Consequently, as the applied force on the SoftSkin increases, so does the deformation of the silicone rubber, resulting in corresponding changes in the sensor signal values.

To achieve accurate and consistent measurement results, a robotic arm (UR5e, Universal Robots, DK) was utilized, equipped with a blunt end-effector and a wrist force and torque sensor (JR3, Woodland, USA). This setup enables the simultaneous application and the measurement of various force magnitudes at specific coordinates on the surface of the SoftSkin prototype.

Fig. 12(a)–(d) illustrates the sensor responses, grouped in four horizontal layers, when subjecting the SoftSkin to different force magnitudes: 5, 15, 30, and 45 N, respectively. Each horizontal layer represents the responses in four adjacent detection zones that measure in the same horizontal plane (see Fig. 3; rows A–D).

With an applied force of 5 N [Fig. 12(a)], the touch signature begins to stand out clearly from the background noise. When the force increases, as shown in Fig. 12(b)–(d), these signatures become increasingly pronounced and clear. Sensor response amplitudes vary layer by layer. As the pressure applied to the silicon rubber increases, we observe a corresponding increase in both the signal amplitude and the detection area from the ToF sensor. However, the mean position of the detection remains unchanged. These initial results demonstrate that SoftSkin sensors can also be used to assess the pressure or force applied.

During the experiments, a systematic increase in contact forces was applied in increments of 3 N (with a penetration depth of corresponding 1 mm). We found that contacts applying a force of 3 N were successfully detected by the ToF sensor within a distance of 20 cm. However, contacts exerting higher force levels of 6 N could be detected over the entire SoftSkin prototype's surface. Based on this data, the contact detection threshold is estimated at around 5 N.

In Fig. 13, the SoftSkin was installed on a cylindrical structure to illustrate its application, for example, on a robotic arm like the UR10 (Universal Robots, DK). The heat map displays a scenario of multitouch feedback. In this instance, the operator touches the sensor skin with two fingers at separate locations simultaneously. Due to the TIR light propagation, the light is only partially reflected at the initial contact point, allowing it to continue and detect subsequent contact points as well.

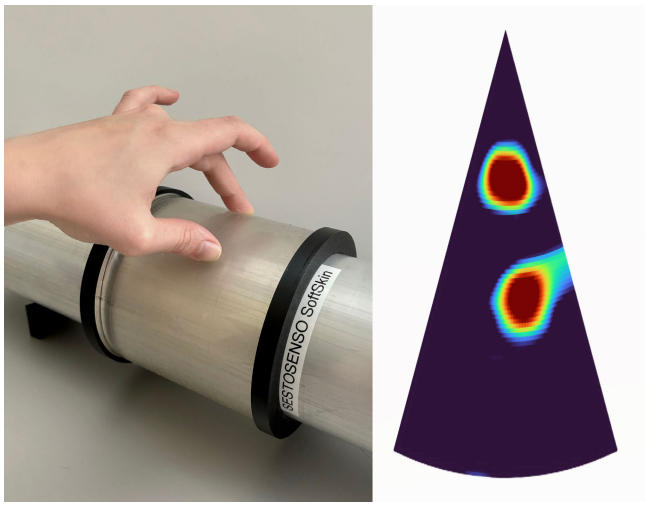

Fig. 13. Usage of the SoftSkin sensor on a cylindrical structure (left) to demonstrate the performance of a single ToF sensor in an application-related scenario. The heat map (right) shows the interpolated sensor response in a situation with multiple contact points and simultaneous localization.

Further, during noncontact situations, it has been observed that OptoSkin sensor's baseline responses exhibit variances between curved and straight geometries. However, upon implementation of our calibration procedure, the baseline offsets are eliminated from the output signal. According to our preliminary assessment, the pressure measurement, which depends on the deformation of the SoftSkin surface, did not reveal any significant discrepancies or deviations in the measurements during this study.

V. Conclusion

We have demonstrated the fundamental principle of our proposed OptoSkin touch sensor through both simulation and experiment. We have developed four different prototypes, each with unique features and capabilities, to showcase the versatility and applicability of our approach. Our results indicate that the proposed sensor is capable of localizing touch events on 1-D (rod) and 2-D surfaces (HardSkin, SoftSkin1, and SoftSkin2), and projecting them onto 2-D and 3D structures. This opens up new possibilities for developing sensors that can detect and respond accurately to touch inputs in various applications.

One of the key advantages of our proposed sensor is its electrode-free surface, which simplifies sensor design and integration. Conventional electrical (resistive or capacitive) touch sensors rely on complex electrode configurations, which can make them difficult and expensive to manufacture and integrate into devices. In contrast, our sensor uses a simple and elegant approach that eliminates the need for electrodes altogether. This not only makes the sensor easier to fabricate but also allows it to conform to irregular surfaces, expanding its potential use cases.

Another advantage of our proposed sensor is its co-located light source and detector. By integrating these two components into a single unit, we can streamline electronics, reduce energy consumption, and improve overall compactness. This is in contrast to traditional touch sensors, which often require separate light sources and detectors, adding to the complexity and cost of the system.

In addition to demonstrating and characterizing pressure/force detection for the first time, our results also highlight the potential of the proposed sensor as a viable alternative to traditional touch sensors. The advantages discussed above make it an attractive option for a wide range of applications, from consumer electronics to medical devices, where accurate and reliable touch sensing is critical.

During our experiments, we have not observed any permanent deformation of our SoftSkin sensors. However, subjecting the SoftSkin surface to excessive tangential forces can lead to damage. Consequently, extra precautions are recommended for such use cases. Our future developments will involve researching sophisticated structures that integrate a protective layer to increase the robustness of the sensor. Notwithstanding, we postulate that, in typical applications, a strong and inflexible surface (HardSkin) will be adequate for detecting contact, with pressure being deducible from the data obtained through the robot's force and torque sensors. From our point of view, the SoftSkin sensor is more suitable for handling fragile and deformable objects, for example.

In the literature, we find various other optical sensors that exhibit 2-D tactile sensitivity. Among others, visual methods are used to detect FTIR [1], [2], [3], [4], [7] or the deformation of a membrane [28], [29], [32], [33], [34], [35] or the imprint of an elastomer layer [30], [36], [37], [38], [39]. Other methods use the detection of free beams using a large number of transmitters and receivers (many-to-many) [31]. In Table IV, we compare various performance characteristics of our OptoSkin sensor with a selection of other optical sensing methods.

We note that vision-based techniques employ a camera to capture visuals of the sensing area and utilize advanced computer-vision algorithms to interpret these images. Due to the vastness of the imaging sensor matrix (ranging from hundreds of thousands to millions of pixels), they typically attain a high spatial resolution in the millimeter domain and some exhibit a high sensitivity to pressure ($\ll$1 N), both of which surpass the capabilities of the OptoSkin. Conversely, the size and frame rate of these images produce a large amount of data that necessitates processing (reading, storage, and analysis). This demands substantial computing power. In contrast, OptoSkin produces minimal data, which can be processed locally on an MCU or in a distributed sensor network [12].

Additionally, vision-based sensors are confined to imaging within a direct line of sight. Therefore, a crucial design variable is the imaging distance d_{im}, which makes the structures quite bulky. In general, the sensing area is limited to a certain surface. Moreover, free-beam sensors necessitate a flat surface. Conversely, OptoSkin enables the customization of the sensor surface to match the application geometry and permits the coverage of larger areas without the need for extra ToF sensors.

Considering the described performance and attributes, other optical surface sensors are designed for specific uses, such as robotic grippers or touch screen displays (touch pads). On the

TABLE IV
SUMMARY OF OPTOSKIN PERFORMANCE AND COMPARISON WITH DIFFERENT OPTICAL TOUCH SENSOR TECHNOLOGIES

Sensor	Description	Sensing area [mm^2]	Thickness	Geometric constraints	Amount of data	Sensory capabilities	
						Touch	Pressure
Time-of-flight sensing of FTIR							
OptoSkin (ours)	Back scattering in wave guide	300×300	Thin	Flat or curved wave guides	$4\times$ 128 byte, 15 Hz (histograms)	Multi, 1 cm	3 N
Vision-based sensing of FTIR							
[7]	Re-propagated multiple reflection path	100×100	Medium	Mirror surfaces	4208 pxl$\times$3120 pxl, 30 Hz (images)	2.3 mm	—
[1]	Imaging of perpendicular scattering	240×240	d_{im}	Planar surface, multi-layer	832 pxl $\times$ 832 pxl, 30 Hz (images)	Multi, 1 mm	0.1 N
Visiflex [4]	Convex multi-layer wave guide	Diam. 30	d_{im}	Specific convex hull	640 pxl $\times$ 480 pxl, 90 Hz (images)	1 mm	0.3 N
Vision-based sensing of surface deformation							
FingerVision [28]	Marker displacement on planar membrane	31×40	d_{im}	Planar membrane	320 pxl $\times$ 240 pxl, 63 Hz (images)	Multi, 1 mm	1 N
TacTip [29]	Marker displacement on convex membrane	Diam. 30-40	d_{im}	Specific convex hull	640 pxl $\times$ 480 pxl, 90 Hz (images)	2 mm	—
GelSight [30]	Deformation of a side-lit elastic layer	Diam. 25	d_{im}	Specific planar multi-layer	320 pxl $\times$ 240 pxl, 30 Hz (images)	0.1 mm	—
Free-beam							
ZeroTouch [31]	Many-to-many free-beam detection	660×1120	Thin	Free space, planar surface	32 emitters, 512 receivers	Multi	—

other hand, our approach involves creating a tactile sensor skin that can be attached to various robot surfaces and conformed to the robot's shape. This facilitates environmental sensing, allowing the robot to maneuver even in complex and dynamic settings or to promote secure HRI.

In conclusion, this article has presented a novel approach to touch sensing that offers several advantages over traditional methods. Through simulation and experimentation, we have shown the fundamental principle behind our proposed sensor, realized four different prototypes, and demonstrated its ability to localize touch events on 1-D and 2-D surfaces and project them onto 2-D and 3-D structures. We believe that this article represents an important step forward in the development of next-generation touch sensors that are simpler, more versatile, and more cost-effective than current technologies.

ACKNOWLEDGMENT

The authors would like to thank the participating institutes for their technical and administrative support of this work.

REFERENCES

[1] S. S. Desai, A. M. Eckert-Erdheim, and A. M. Hoover, "A large-area tactile force sensor for measuring ground reaction forces from small legged robots," in *Proc. IEEE/RSJ Int. Conf. Intell. Robots Syst.*, Nov. 2013, pp. 4753–4758.

[2] A. K. B. Mahmood and S. Sulaiman, "Design and implementation of multi-touch system using FTIR technique for optimization of finger touch detection," in *Proc. Int. Symp. Inf. Technol.*, vol. 1, Jun. 2010, pp. 1–7.

[3] J. Y. Han, "Low-cost multi-touch sensing through frustrated total internal reflection," in *Proc. UIST*. New York, NY, USA: Association for Computing Machinery, 2005, pp. 115–118, doi: 10.1145/1095034.1095054.

[4] A. J. Fernandez, H. Weng, P. B. Umbanhowar, and K. M. Lynch, "Visiflex: A low-cost compliant tactile fingertip for force, torque, and contact sensing," *IEEE Robot. Autom. Lett.*, vol. 6, no. 2, pp. 3009–3016, Apr. 2021.

[5] S. Hodges, S. Izadi, A. Butler, A. Rrustemi, and B. Buxton, "ThinSight: Versatile multi-touch sensing for thin form-factor displays," in *Proc. 20th Annu. ACM Symp. User Interface Softw. Technol.*, Oct. 2007, pp. 259–268.

[6] R. Hofer, D. Naeff, and A. Kunz, "FLATIR: FTIR multi-touch detection on a discrete distributed sensor array," in *Proc. 3rd Int. Conf. Tangible Embedded Interact.*, Feb. 2009, pp. 317–322.

[7] R. Wattanaparinton and K. Takemura, "Vision-based tactile sensing using multiple contact images generated by re-propagated frustrated total internal reflections," in *Proc. IEEE Int. Conf. Syst., Man, Cybern. (SMC)*, Oct. 2022, pp. 962–967.

[8] P. Piacenza et al., "Accurate contact localization and indentation depth prediction with an optics-based tactile sensor," in *Proc. IEEE Int. Conf. Robot. Autom. (ICRA)*, Singapore, May 2017, pp. 959–965.

[9] B. Jarrahi and J. Wanek, "Design of an fMRI-compatible optical touch stripe based on frustrated total internal reflection," in *Proc. 36th Annu. Int. Conf. IEEE Eng. Med. Biol. Soc.*, Aug. 2014, pp. 4952–4955.

[10] J. Hirano and D. Garmire, "Force transducer through total internal reflection and frustrated total internal reflection for a three-axis anemometer," *IEEE Sensors J.*, vol. 15, no. 7, pp. 3827–3834, Jul. 2015.

[11] J.-T. Lin, C. A. Newquist, and C. K. Harnett, "Multitouch pressure sensing with soft optical time-of-flight sensors," *IEEE Trans. Instrum. Meas.*, vol. 71, pp. 1–8, 2022.

[12] F. Giovinazzo, F. Grella, M. Sartore, M. Adami, R. Galletti, and G. Cannata, "From CySkin to ProxySKIN: Design, implementation and testing of a multi-modal robotic skin for human–robot interaction," *Sensors*, vol. 24, no. 4, p. 1334, Feb. 2024.

[13] F. Piron, D. Morrison, M. R. Yuce, and J.-M. Redouté, "A review of single-photon avalanche diode time-of-flight imaging sensor arrays," *IEEE Sensors J.*, vol. 21, no. 11, pp. 12654–12666, Jun. 2021.

[14] M. Born and E. Wolf, *Principles of Optics: Electromagnetic Theory of Propagation, Interference and Diffraction of Light*. Amsterdam, The Netherlands: Elsevier, 2013.

[15] P. F. McManamon, *Field Guide to LiDAR*, vol. FG36. Bellingham, WA, USA: SPIE Press, 2015.

[16] U. Wandinger, *Introduction to LiDAR*. Cham, Switzerland: Springer-Verlag, 2005, pp. 1–18.

[17] M. Van Gemert, S. Jacques, H. Sterenborg, and W. Star, "Skin optics," *IEEE Trans. Biomed. Eng.*, vol. 36, no. 12, pp. 1146–1154, Dec. 1989.

[18] T. Kono and J. Yamada, "In vivo measurement of optical properties of human skin for 450–800 nm and 950–1600 nm wavelengths," *Int. J. Thermophys.*, vol. 40, no. 5, pp. 1–14, May 2019.

[19] A. Lavatelli, A. Zanoni, E. Zappa, and A. Cigada, "On the design of force sensors based on frustrated total internal reflection," *IEEE Trans. Instrum. Meas.*, vol. 68, no. 10, pp. 4065–4074, Oct. 2019.

[20] W. Jakob et al. (2022). *Mitsuba 3 Renderer*. [Online]. Available: https://mitsuba-renderer.org

[21] A. Jarabo, J. Marco, A. Muñoz, R. Buisan, W. Jarosz, and D. Gutierrez, "A framework for transient rendering," *ACM Trans. Graph.*, vol. 33, no. 6, pp. 1–10, Nov. 2014.

[22] D. Royo, J. García, A. Muñoz, and A. Jarabo, "Non-line-of-sight transient rendering," *Comput. Graph.*, vol. 107, pp. 84–92, Oct. 2022. [Online]. Available: https://www.sciencedirect.com/science/article/pii/S0097849322001200

[23] F. Foschum, F. Bergmann, and A. Kienle, "Precise determination of the optical properties of turbid media using an optimized integrating sphere and advanced Monte Carlo simulations. Part 1: Theory," *Appl. Opt.*, vol. 59, no. 10, p. 3203, 2020.
[24] F. Bergmann, F. Foschum, R. Zuber, and A. Kienle, "Precise determination of the optical properties of turbid media using an optimized integrating sphere and advanced Monte Carlo simulations. Part 2: Experiments," *Appl. Opt.*, vol. 59, no. 10, p. 3216, 2020.
[25] Metricon. *MODEL 2010/ M OVERVIEW*. Accessed: Apr. 24, 2024. [Online]. Available: https://www.metricon.com/model-2010-m-overview
[26] L. Cauchy, "Sur la dispersion de la Lumiere," *Bulletin des Sci. Mathématiques*, vol. 14, p. 9, Jan. 1830.
[27] AMS-OSRAM. (2023). *DS000693 TMF8820/21/28 Multizone Time-of-Flight Sensor*. Accessed: Apr. 24, 2024. [Online]. Available: https://look.ams-osram.com/m/52236c476132a095/original/TMF8820-21-28-Multizone-Time-of-Flight-Sensor.pdf
[28] A. Yamaguchi and C. G. Atkeson, "Implementing tactile behaviors using FingerVision," in *Proc. IEEE-RAS 17th Int. Conf. Humanoid Robot. (Humanoids)*, Nov. 2017, pp. 241–248.
[29] B. Ward-Cherrier et al., "The TacTip family: Soft optical tactile sensors with 3D-printed biomimetic morphologies," *Soft Robot.*, vol. 5, no. 2, pp. 216–227, Apr. 2018.
[30] R. Li et al., "Localization and manipulation of small parts using GelSight tactile sensing," in *Proc. IEEE/RSJ Int. Conf. Intell. Robots Syst.*, Sep. 2014, pp. 3988–3993.
[31] J. Moeller and A. Kerne, "ZeroTouch: An optical multi-touch and free-air interaction architecture," in *Proc. SIGCHI Conf. Human Factors Comput. Syst.*, May 2012, pp. 2165–2174.
[32] K. He, X. Shi, D. Yu, and X. Guo, "Vision-based high-resolution tactile sensor by using visual light ring," *IEEE Sensors Lett.*, vol. 6, no. 4, pp. 1–4, Apr. 2022.
[33] Y. Zhang, Z. Kan, Y. Yang, Y. A. Tse, and M. Y. Wang, "Effective estimation of contact force and torque for vision-based tactile sensors with Helmholtz–Hodge decomposition," *IEEE Robot. Autom. Lett.*, vol. 4, no. 4, pp. 4094–4101, Oct. 2019.
[34] C. Trueeb, C. Sferrazza, and R. D'Andrea, "Towards vision-based robotic skins: A data-driven, multi-camera tactile sensor," in *Proc. 3rd IEEE Int. Conf. Soft Robot. (RoboSoft)*, New Haven, CT, USA, May 2020, pp. 333–338.
[35] J. Bewley, G. P. Jenkinson, and A. Tzemanaki, "Optical-tactile sensor for lump detection using pneumatic control," *Frontiers Robot. AI*, vol. 8, Jul. 2021, Art. no. 672315.
[36] W. Yuan, S. Dong, and E. Adelson, "GelSight: High-resolution robot tactile sensors for estimating geometry and force," *Sensors*, vol. 17, no. 12, p. 2762, Nov. 2017.
[37] D. F. Gomes, Z. Lin, and S. Luo, "GelTip: A finger-shaped optical tactile sensor for robotic manipulation," in *Proc. IEEE/RSJ Int. Conf. Intell. Robots Syst. (IROS)*, Oct. 2020, pp. 9903–9909.
[38] H. Jiang, Y. Yan, X. Zhu, and C. Zhang, "A 3-D surface reconstruction with shadow processing for optical tactile sensors," *Sensors*, vol. 18, no. 9, p. 2785, Aug. 2018.
[39] Y. Zhang, X. Chen, M. Y. Wang, and H. Yu, "Multidimensional tactile sensor with a thin compound eye-inspired imaging system," *Soft Robot.*, vol. 9, no. 5, pp. 861–870, Oct. 2022.

Emmanuel Bacher received the Higher National Diploma degree in electrical and industrial computer science from the University of Haute-Alsace, Mulhouse, France, in 1993, and the M.Sc. degree in experimental physics from the Conservatoire national des arts et métiers, Mulhouse, France, in 2001.

He is a Research Engineer in the Advanced Visionics and Processing Group of the French-German Research Institute of Saint-Louis (ISL), Saint-Louis, France. He is responsible for conducting experimental trials, automating experimental equipment, and designing integrated electronic circuits.

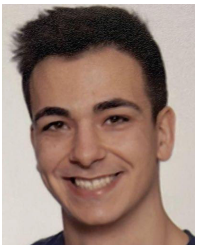

Sergio Cartiel received the master's degree in robotics, graphics and computer vision from the University of Zaragoza, Zaragoza, Spain, in 2024.

He is currently a Junior Researcher with the Graphics and Imaging Laboratory, University of Zaragoza. His main research interests are light transport simulation, including time-resolved light transport, computational imaging, and adaptive numerical integration methods.

Jorge García-Pueyo received the master's degree in robotics, graphics and computer vision from the University of Zaragoza, Zaragoza, Spain, in 2024.

He is a Junior Researcher with the Graphics and Imaging Laboratory, University of Zaragoza. His main research interests are light transport simulation, including time-resolved light transport and computational imaging, with a focus on forward and inverse problems.

Julija Stopar received the master's degree in electrical engineering from the University of Ljubljana, Ljubljana, Slovenia, in 2023.

She is currently employed as a Researcher with the Laboratory of Robotics, University of Ljubljana. Her research interests lie primarily in the field of artificial intelligence, robotics, and information communication technologies.

Aleš Zore received the master's degree in electrical engineering from the University of Ljubljana, Ljubljana, Slovenia, in 2017.

He is currently a Researcher with the Faculty of Electrical Engineering, University of Ljubljana. His latest research focuses are the development of adaptive robotic cell and the development of SoftSkin for human–robot enhanced safety.

Roman Kamnik (Member, IEEE) received the D.Sc. degree in electrical engineering from the Faculty of Electrical Engineering, University of Ljubljana, Ljubljana, Slovenia, in 1999.

He is currently a Senior Researcher with the Laboratory of Robotics and a Full Professor with the Faculty of Electrical Engineering, University of Ljubljana. His research interests are focused on biomedical engineering and robotics. He specializes in the development of intelligent robotic devices with applications in sports, industrial and rehabilitation robotics, and transport.

Ilze Aulika received the Ph.D. degree from the University of Latvia (UL), Riga, Latvia, in 2008.

She is a Leading Researcher with the Institute of Solid State Physics (ISSP), UL, and also a Solid-State Physicist with a diverse background in research and industry, and expertise in experimental physics, material science, and thin film technologies. She is one of the time-of-flight (ToF)-based optical tactile sensor inventors; underpinned the Sestosenso Project (Grant number 101070310) to realize this concept jointly with ISL, UZ, and UL. Her current research interests include in situ optical investigations of thin films/multilayers for smart windows and organic light-emitting diodes (OLED), and IR light interaction with the matter for ToF advanced applications.

Andrejs Ogurcovs received the Ph.D. degree from Daugavpils University, Daugavpils, Latvia, in 2017, specializing in solid-state physics.

He is a Researcher with the Institute of Solid State Physics (ISSP), University of Latvia (UL), Riga, Latvia. His research focus is the development of metal–oxide nanostructure-based electrochemical sensor systems for detecting organic and inorganic substances and optical tactile transduction based on time-of-flight (ToF) investigations. His expertise includes proficiency in atomic force microscopy, electrochemistry, hydrothermal synthesis, and electronic hardware/software design for biosensor and optical skin applications.

Jurģis Grūbe received the Ph.D. degree from the University of Latvia (UL), Riga, Latvia, in 2005, with a specialization in solid-state spectroscopy.

He is a Leading Researcher with the Institute of Solid State Physics (ISSP), University of Latvia (UL), Riga, Latvia. His research primarily focuses on upconversion luminescence in diverse materials, including micro- and nanoparticles. He investigates luminescence decay kinetics and explores energy-transfer mechanisms that contribute to luminescence. His expertise includes luminescence and exciton spectroscopy, absorption, transmission, reflectance spectra, and spectroscopic experimental setup design.

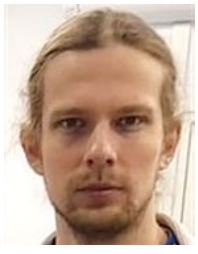

Arturs Bundulis received the Ph.D. degree from the University of Latvia (UL), Riga, Latvia, in 2020.

He is a Senior Researcher with the Institute of Solid State Physics (ISSP), UL, and specializes in 2nd-/3rd-order nonlinear optical (NLO) studies of organic materials and their application in integrated photonics. His research encompasses structure-property relations, fundamental aspects of nonlinear effects, and NLO properties of plasmonic structures for photonic applications. Notably, he works on the development of integrated polymer photonics based on host-guest systems for frequency comb and quantum light source development.

Jelena Butikova received the Ph.D. degree in solid state physics from the University of Latvia (UL), Riga, Latvia, in 2009.

She is a Senior Researcher with the Laboratory of Spectroscopy, Institute of Solid State Physics (ISSP), UL. She is responsible for the spectroscopic ellipsometer (SE), and she has experience in SE and expertise in laser spectroscopic methods.

Meldra Kemere received the Ph.D. degree in natural sciences with a specialization in solid-state spectroscopy from the University of Latvia (UL), Riga, Latvia, in 2023.

She is a Researcher with the Laboratory of Spectroscopy, Institute of Solid State Physics (ISSP), UL. She has experience in the optical characterization of various materials including glass-ceramics, polycrystalline, and polymer materials. Her expertise comprises luminescence and time-resolved measurements, and the characterization of light transmission and reflection in materials.

Adolfo Muñoz defended his Ph.D. thesis “Light Transport in Participating Media” which established his original research topics: light transport simulation and capture and modeling of material appearance, in April 2010.

He is an Associate Professor with the Department of Computer Science and Systems Engineering, Universidad de Zaragoza, Zaragoza, Spain, where he belongs to the Graphics and Imaging Laboratory. More recently, he has incorporated other interests such as computational and transient imaging.

Martin Laurenzis received the master’s degree in physics from TU Dortmund University, Dortmund, Germany, in 1999, and the Ph.D. degree in electrical engineering and information technology from RWTH Aachen University, Aachen, Germany, in 2005.

Since 2004, he has been working with the French-German Research Institute of Saint-Louis (ISL), Saint-Louis, France, and is currently a Senior Research Fellow. After working on semiconductor electronics and optical data storage, his research interests turned to laser-based imaging, with a focus on 3-D imaging, computational imaging techniques such as non-line-of-sight (NLOS) imaging, and the application of single-photon countering devices.